Journal of Energy Storage 40 (2021) 102756

Contents lists available at ScienceDirect

Journal of Energy Storage

journal homepage: www.elsevier.com/locate/est

Fast charging for electric vehicles applications: Numerical optimization of a multi-stage charging protocol for lithium-ion battery and impact on cycle life

Romain Mathieu [a,*], Olivier Briat [a], Philippe Gyan [b], Jean-Michel Vinassa [a]

[a] Univ. Bordeaux, CNRS, Bordeaux INP, IMS, UMR 5218, F-33400, Talence, France
[b] Renault, FR TCR LAB 012, Technocentre de Guyancourt, 1 Avenue du Golf, 78084, Guyancourt, France

ARTICLE INFO

Keywords:
Electric vehicles
Fast charge
Numerical optimization
Aging
Lithium-ion battery
Temperature dependency

ABSTRACT

One challenge of fast charging for electric vehicles is the potential degradation caused by high charge currents on the battery. This article focuses on the numerical optimization of fast charging protocols and on their impact on battery cycle life. An optimization problem is formulated to define the parameters of a multi-stage of constant current charging protocol. The problem is based on a strongly coupled electro-thermal model and is developed to achieve fast charging while taking aging into account in an implicit manner.

The proposed method is used to define optimized protocols in different operating conditions in terms of ambient temperature, charging time, and charged capacity. Experimental aging tests are then conducted to investigate their impact on the cycle life of a lithium-ion cell. Optimized protocols are compared with fast charging reference protocols in similar operating conditions. The results show that the optimized protocols can reduce the charging time and/or the degradation compared to the reference protocols. This indicates that there exist opportunities for significantly higher currents to reduce battery charging time while still maintaining a long cycle life.

1. Introduction

Fast charging of lithium-ion batteries is an important step towards the adoption of electric vehicles. The deployment of very high power charging systems is underway in several regions thanks to the coordination of both public and private actors [1]. This current deployment motivates many research works on the battery side, to make lithium-ion batteries accept higher charging power and effectively reduce charging times [2,3]. This paper focuses on the issue of optimized fast charging protocols.

The charging protocol controls current, voltage, and/or power during the charging stage of batteries [4]. In general, the goal of optimized fast charging protocols is to find the best compromise between a low charging time, a high energy charged, and a high durability [5], which are contradictory objectives. In particular, durability has to be carefully considered because high charge currents rates are often considered as a factor of aging acceleration [5–7]. The reason comes from several aging mechanisms such as lithium plating [8], solid electrolyte interphase (SEI) growth [9] and mechanical degradation [10,11]. These mechanisms depend strongly on battery states such as state-of-charge (SOC), temperature and state-of-health (SOH). Thus, parameters of charging protocols should vary depending on the operating conditions.

Therefore, optimized fast charging protocols seek to design the charge current or power profile with the highest rates possible that minimizes aging. Two key questions are raised. The first one concerns the choice of a charging protocol, which determines the charge current or power profile. The second one concerns the definition of its parameters, which decide the value of charge current or power. While considering the choice of a protocol, many have been proposed in the literature such as constant current–constant voltage (CC–CV) protocols [5,12], multi-stage of constant current (MSCC) protocols [13,14], pulse-charging protocols [13,15], and unconstrained protocols or protocols that follow a defined trajectory [15–17]. While considering the definition of optimized charging protocols parameters, they are two main approaches in the literature: experimental and numerical. The experimental approach seeks to observe an experimental criterion whose value limits the charge current or power. It involves methods such as three-electrode tests [18–20], mechanical activity monitoring [21], voltage relaxation tests [22], or design-of-experiments [15,23,24]. The numerical approach is based on a mathematical model of battery behavior and on numerical optimization methods. This paper considers the numerical optimization approach, because it is well suited for the intrinsic compromise that fast charging protocols have to offer.

* Corresponding author.
E-mail address: romain_mathieu@ymail.com (R. Mathieu).

https://doi.org/10.1016/j.est.2021.102756
Received 15 January 2021; Received in revised form 12 April 2021; Accepted 22 May 2021
Available online 31 May 2021
2352-152X/© 2021 Elsevier Ltd. All rights reserved.

It also has the ability to rapidly define protocols for many operating conditions.

Several contributions to the definition of charging protocols by numerical optimization have been published in the literature [14,16,17,25–28]. They differ by the underlying model used, the optimization problem and the realization of experimental aging tests or lack thereof. The aforementioned articles bring notable improvements; however, in our perspective, there remains several issues that limit their potential for defining fast charging protocols in real electric vehicle applications. The main issue concerns the impact of these protocols on the cycle life of lithium-ion batteries. Some studies did not realize experimental aging tests [25–27]. Therefore, the impact of such optimized protocols on aging was not validated experimentally. Lin et al. realized such experimental tests; however, they did not provide detailed information on the cell used [28]. Thus, the results cannot be interpreted comprehensively because the electrode materials and energy density of the cell are not known, although they strongly influence aging [29]. Three studies provided more information on aging. Perez et al. observed that the optimized protocol increased the degradation compared to a reference CC–CV protocol with a similar charging time [17]. Guo et al. witnessed that the optimized protocol allowed to decrease the degradation compared to a reference CC–CV protocol [16]. Yet, the charging time of the reference protocol was significantly inferior, which skews the comparison. Zhang et al. observed that the optimized protocol caused a similar degradation compared to a reference CC–CV protocol, for a charging time divided by two [14]. Nevertheless, the charging time of the optimized protocol is still superior to one hour, which is high for the high power cell that is investigated and cannot be considered as fast charging [5,30]. Consequently, in our opinion, there is a need for additional experimental aging data to demonstrate the applicability of such optimized protocols for electric vehicles.

The objective of our study is to experimentally investigate the possibility to define protocols, that limit the impact of fast charging on battery lifetime, by numerical optimization. To fulfill this objective, this paper reports on a numerical optimization method that we developed and further used to define fast charging protocols. Then, the degradation that these protocols induce is experimentally compared on a high energy cell with reference CC–CV protocols, that were investigated in one of our previous studies [31], and under similar operating conditions. Section 2 details the numerical background and the optimization problem developed to define the parameters of a MSCC charging protocol. Section 3 presents the experimental aging tests achieved to verify the impact on cycle life of the optimized protocols. Finally, Section 4 reports and discusses the degradation results by comparing the optimized protocols with reference CC–CV protocols.

2. Optimization problem and numerical results

This section first justifies the choice of the protocol and presents the underlying model used for simulating battery behavior. Then, it describes the formulation of the optimization problem and shows examples of numerical results.

2.1. Multi-step of constant current (MSCC) charging protocol

We choose to optimize the charge based on a multi-stage of constant current protocol (MSCC). Fig. 1 illustrates its principle. The charging process is separated in n stages of constant current (CC) $[I_1, I_2, \dots, I_n]$, which are combined with n voltage thresholds $[U_1, U_2, \dots, U_n]$, which control the end of each CC stage. The end of stages can also be controlled by SOC thresholds $[SOC_1, SOC_2, \dots, SOC_n]$. In this article, voltage thresholds are preferred as they do not need to be adapted to a decreasing capacity unlike SOC thresholds.

The MSCC protocol can be used with progressively increasing U_i thresholds such as illustrated in Fig. 1. In this case, its principle is to apply different charge current rates depending on the SOC range.

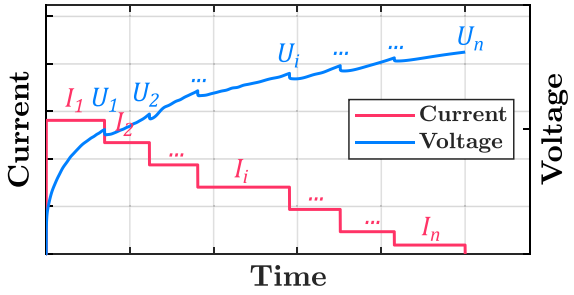

Fig. 1. Theoretical illustration of current (red) and voltage (blue) profiles vs. time during a MSCC protocol with current stages delimited by voltage thresholds. (For interpretation of the references to color in this figure legend, the reader is referred to the web version of this article.)

Proceeding this way, the MSCC protocol allows a finer tuning than the CC–CV protocol [32]. In particular, it can decrease the current in the last stages of the charging process to avoid aging mechanisms that are amplified by high SOC, such as lithium plating [18,21]. An unconstrained protocol or a protocol following a current trajectory can also provide this advantage. However, the definition of the MSCC protocol parameters is simplified and is well suited to a numerical optimization problem. Moreover, the straightforward structure of this protocol promotes its implementation into electric vehicle charging systems. For all these reasons, we expect the MSCC protocol to provide good performances for fast charging optimization.

2.2. Coupled electro-thermal model

To represent the battery behavior during charge, an electrical model is coupled with thermal dynamics. The framework of the coupled electro-thermal model used is based on existing works in the literature [33–35]. This subsection thus briefly describes its main equations and its parameterization methods.

The electrical model is an equivalent circuit model. It computes the evolution of the cell voltage U (in volts) in relation to the applied current I (in amperes, a positive current convention in charge is considered) during time t. The cell voltage is expressed with three terms as

$$U = U_{oc} + \eta_\Omega + \sum_{j=1}^{n} \eta_j. \tag{1}$$

The first term is the open-circuit voltage U_{oc}. It is mainly a function of the state-of-charge SOC. The SOC is computed according to Eq. (2), where SOC_{ini} is the initial SOC and Q_c is the cell capacity (in Ah). As the coulombic efficiency of lithium-ion cells is generally high (superior to 99%), it can be ignored in Eq. (2) without significant errors in SOC estimation because the model is only used in this study to simulate a single charge. The second term is the ohmic overvoltage η_Ω. Its value is computed by Eq. (3), where R_Ω is a series resistor representing the cell ohmic resistance. This resistance is a function of the cell temperature. The third term is the polarization overvoltage, accounting for charge transfer, electrochemical double layer and diffusion phenomenon. It is represented in the equivalent circuit by a series of R–C parallel circuits of voltage η_j and time constants $\tau_j = R_j C_j$. They account for transient dynamics and the voltage drop over each circuit is described by Eq. (4). In this study, three R–C parallel circuits are used for a good trade-off between low computation time and high precision as recommended in [36]. The value of time constants τ_j are fixed and the resistances R_j are considered as a function of cell temperature, SOC, current rate

and direction of the current (charge or discharge).

$$SOC = SOC_{ini} + \frac{1}{3600 Q_c} \int I \mathrm{d}t. \tag{2}$$

$$\eta_\Omega = R_\Omega I. \tag{3}$$

$$\tau_j \frac{\mathrm{d}\eta_j}{\mathrm{d}t} = -\eta_j + R_j I. \tag{4}$$

The thermal model is a one-state lumped-parameters model. It computes the evolution of the cell temperature T_c (in kelvins) depending on the ambient temperature T_{ext} and generated heat $\dot{Q}_{gen}$ (in watts) as described by

$$mC_p \frac{\mathrm{d}T_c}{\mathrm{d}t} = \dot{Q}_{gen} + hS\left(T_{ext} - T_c\right), \tag{5}$$

where C_p (in J K^{-1} kg^{-1}) is the cell specific heat capacity, m (in kg) is the cell mass, S (in m^2) is the cell external surface and h (in W K^{-1} m^{-2}) is the heat transfer coefficient between the cell and its outside environment, which accounts for thermal exchanges by convection, radiation and conduction. The generated heat $\dot{Q}_{gen}$ is described by Eq. (6). The first term corresponds to joule heat and comes directly from the electrical model. The second term corresponds to entropy heat, where the coefficient $\frac{\partial U_{oc}}{\partial T}$ is a function of SOC.

$$\dot{Q}_{gen} = I\left(U - U_{oc}\right) + IT_c \frac{\partial U_{oc}}{\partial T}. \tag{6}$$

A high energy 3 Ah 18 650 cell is considered throughout this article. The cell is further presented in the experimental section (refer to 3.1). Several methods from the literature were used to identify the model parameters. The open-circuit voltage U_{oc} and cell capacity Q_c were identified during an incremental charge with relaxation periods [37]. The resistances R_Ω, R_j and time constants τ_j were identified during electrochemical impedance spectroscopy tests as well as charge/discharge pulses and relaxations tests [33]. These tests were realized at several temperatures (between −15 °C and 45 °C), several SOC (between 0 % and 100 %) and several current values (between 1.5 A and 7.5 A), to obtain a lookup table of impedance parameters values at different operating conditions. Specific heat capacity C_p and heat transfer coefficient h were obtained during a heating test by application of a squared alternative current [38]. Finally, the entropy heat coefficient $\frac{\partial U_{oc}}{\partial T}$ was identified during potentiometric measurements of open-circuit voltage at different temperatures and SOC [39]. Calibration procedure of the electro-thermal model and identified parameters are further described in supplementary materials (refer to Appendix).

Based on the described models, a simulator is coded into the Simulink environment. The functional coupling between electrical and thermal models is illustrated by Fig. 2 and works as described in the following. Depending on the applied current, the electrical model first computes SOC and U based on values of U_{oc}, R_Ω and R_i at this SOC and T_c. The values of SOC, U_{oc} and U are then passed onto the thermal model, which computes $\dot{Q}_{gen}$ and then T_c. The value of T_c finally comes back into the electrical model to compute the new values of resistances parameters. Upstream from the coupled electro-thermal model, a charge controller block is integrated to determine the applied current based on a CC–CV or MSCC protocol.

To verify the model validity for the study of fast charging, experimental CC–CV charges at three current values (1.5, 3.0 and 6.0 A, corresponding to C/2, 1C and 2C) and at three ambient temperatures (0, 20 and 40 °C) were realized and compared to simulation results. Comparison results are given as supplementary files to this article (refer to Appendix). Results show that the model accurately predicts the cell voltage (with an error range of 24–46 mV), as well as the cell temperature (with an error range of 0.2–1.2 °C) and charging time for the 9 tests. Hence, the coupled electro-thermal model is suited to our investigation of fast charging at different temperatures.

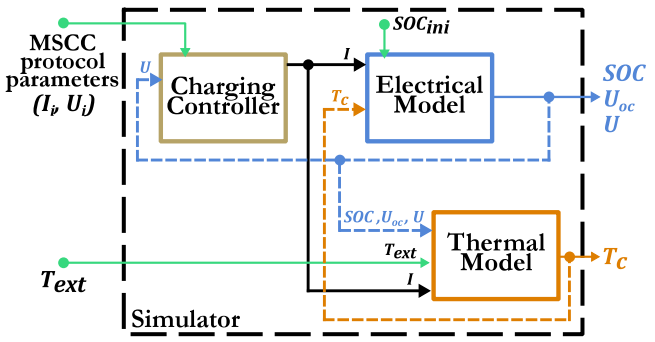

Fig. 2. Schematic representation of the simulator developed to emulate battery behavior during MSCC charge.

2.3. Constrained optimization problem

This subsection formulates a constrained optimization problem [40] to define the parameters of a MSCC charging protocol, using the battery model described above. No aging model is used in this article; instead, battery aging is taken into account in an implicit manner, in the different costs and constraints. Proceeding this way allows to promptly reuse its results for another cell reference, without needing to calibrate a new aging model.

2.3.1. Costs

Costs are mathematical functions to be minimized. In the literature on optimized charging protocol cited in the introduction, several costs are frequently considered. All references used a cost on charging time [14,16,17,25–28], two used a cost on energy losses during charging [25,27], three used a cost on cell temperature rise [14,25,26], and three used a cost on cell degradation when using an aging model [17,27,28]. In the present paper, charging time is rather chosen as a constraint and two distinct costs are considered. These two cost functions are dependent on the vector of optimization variables $\vec{x}$, which are the currents of each step of the MSCC protocol.

The first cost is a cost on energy losses J_{el} due to joule effect, which exists in the literature. This cost is computed by integration of overvoltages during the whole charge duration as expressed by Eq. (7). The effect of J_{el} is to reduce the charging current and it is more important when the internal resistance is higher, such as at low SOC and low temperatures [33].

$$J_{el}\left(\vec{x}\right) = \int_{t_0}^{t_f} \left(U(t) - U_{oc}(t)\right) I(t)\mathrm{d}t. \tag{7}$$

The second cost is a cost on end-of-charge overvoltages J_{eoc}. Relative to existing literature, it is a novel proposition to limit aging mechanisms accelerated by fast charging at high SOC such as lithium plating or SEI growth. To determine what SOC range corresponds to the final part of the charge for a given cell, we propose to use differential voltage analysis [41] from a low current charge as plotted on Fig. 3 for the studied cell. Several distinctive features of the positive and negative electrodes can be observed on Fig. 3b. More specifically, the position of the central graphite peak is highlighted. This peak corresponds to a half-lithiated graphite (LiC_{12}), and signals the start of the potential plateau corresponding to the transition of graphite from this stage to the fully lithiated stage (LiC_6) [42]. As this plateau is the closest to the potential of lithium plating, the position of the central graphite peak can be used as a signal for the beginning of the last part of charging. This peak is positioned at 50% of graphite SOC, but can change for the full cell depending on the balancing between positive and negative electrodes. For the studied cell, it is located at 57% (Fig. 3b). The cost J_{eoc} is finally computed with Eq. (8), by an integration in the SOC domain of overvoltages multiplied by a penalty function P_{eoc}. This

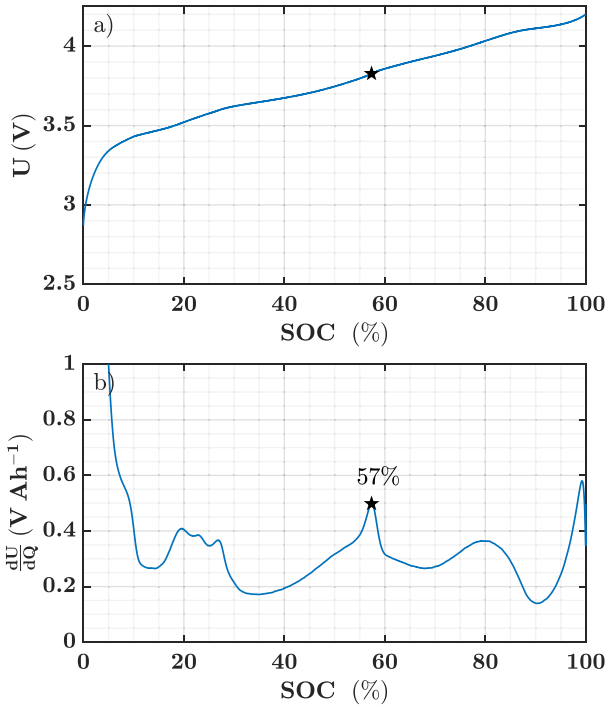

Fig. 3. Position of the LiC_{12} graphite peak on the SOC scale: (a) cell voltage during a C/10 charge at 25 °C and (b) corresponding differential voltage with position of central graphite peak highlighted.

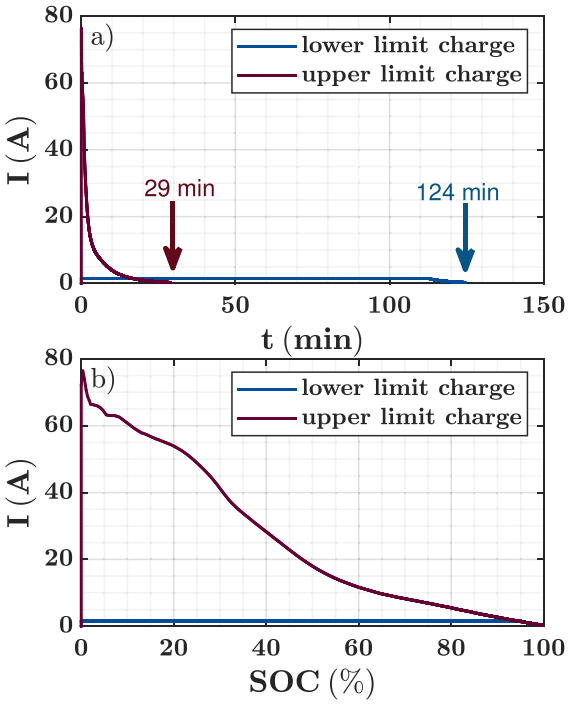

Fig. 4. Limits on optimal charge search: simulated current profiles of lower limit charge and upper limit charge as a function of (a) time and (b) SOC (example at 25 °C). The reader is advised that the upper limit charge leads to an extremely high current peak at the beginning of charge and should be considered as a theoretical case (here simulated), as charging a cell at such rates could lead to safety issues.

penalty function is calculated by Eq. (9), where γ_{SOC} is the SOC of the central graphite peak as highlighted on Fig. 3b. Thus, the effect of J_{eoc} is to reduce the charge current after the beginning of last graphite transition and it increases towards higher SOC.

$$J_{eoc}\left(\vec{x}\right) = \int_{SOC_0}^{SOC_f} \left(U(SOC) - U_{oc}(SOC)\right) P_{eoc}(SOC)\mathrm{d}SOC. \tag{8}$$

$$P_{eoc}\left(SOC\right) = \begin{cases} 0, & \text{if } SOC < \gamma_{SOC}, \\ \left(SOC - \gamma_{SOC}\right)^3, & \text{if } SOC \geq \gamma_{SOC}. \end{cases} \tag{9}$$

As expressed by Eqs. (7) and (8), the two cost functions J_{el} and J_{eoc} can have very different numerical values, which can be delicate to balance. To avoid this issue, we propose to normalize them by introducing limits on the optimal charge to be found. An inferior limit would be a normal charge, with a charging time just below of what could be considered as fast charging. For a high energy cell as the one studied, we choose a CC–CV protocol with a current rate of C/2 (meaning here a current of 1.5 A) for a slowest charge possible of around 2 h. A superior limit would be the fastest charge possible. Of all conceivable definitions, the highest current profile possible without exceeding the upper voltage limit of the cell (here 4.2 V) is chosen. This can be obtained by achieving a CV charge directly from the discharged state. These two charges can be simulated with the model and Fig. 4 represents their obtained current profiles in the time and SOC domains. The defined upper limit charge leads to extremely high currents which would not be safe for the cell. This charge should thus be considered as a theoretical high limit for current and low limit for charging time (here 29 min at 25 °C). These two charge limits can be simulated for each simulation condition to obtain the value of $J_{i,lb}$ and $J_{i,ub}$, where J_i is either J_{el} or J_{eoc}. These values finally allow to normalize the cost function with Eq. (10). The normalized costs $\tilde{J}_i$ thus vary between 0 and 1. Consequently, the optimal fast-charge protocol should have a current profile that is between the two curves on Fig. 4b, for a charge duration between the two bounds on Fig. 4a.

$$\tilde{J}_i = \frac{J_i - J_{i,lb}}{J_{i,ub} - J_{i,lb}}. \tag{10}$$

The next step is to construct the objective function f that is to be minimized by weighting the individual costs as expressed by

$$f\left(\vec{x}\right) = \omega_{el}\tilde{J}_{el} + \omega_{eoc}\tilde{J}_{eoc}, \tag{11}$$

where ω_{el} and ω_{eoc} are the weights respective to costs $\tilde{J}_{el}$ and $\tilde{J}_{eoc}$. The vector of weights is noted $\vec{\omega} = [\omega_{el}, \omega_{eoc}]$. Fig. 5 reports the evolution of the individual cost functions versus the CC current of CC–CV charge protocol in the range 1.5 A (C/2) to 9 A (3C). It can be observed that the cost $\tilde{J}_{eoc}$ is higher and increases faster with charge current compared to the cost $\tilde{J}_{el}$. Thus, it is possible to use a higher weight on $\tilde{J}_{el}$ to balance the two objectives.

Due to their numerical nature, the allocation of weights requires prior numerical experiments and should depend on the relative importance of cost $\tilde{J}_{el}$ and $\tilde{J}_{eoc}$ to the user of the method. As we stated for the costs in Section 2.3.1, allocating a higher weight ω_{el} will tend to reduce the current more towards low SOCs, whereas allocating a higher weight ω_{eoc} will tend to reduce the current more towards high SOCs. Ultimately, we chose to allocate a higher weight on $\tilde{J}_{el}$ to put an emphasis on relatively higher currents towards higher SOCs because for real electric vehicle, charging will rarely start from very low SOCs, which limits the benefits of charging protocols that make use of very high current values at low SOCs to reduce total charging time (such as those resulting from a higher weight on $\tilde{J}_{eoc}$ here). All in all, the weights $\vec{\omega} = [0.8,\ 0.2]$ are used in the rest of this article.

2.3.2. Constraints

With the objective function defined, we propose a constrained optimization problem to determine the parameters of a MSCC fast charging protocol. The considered problem is expressed as follows

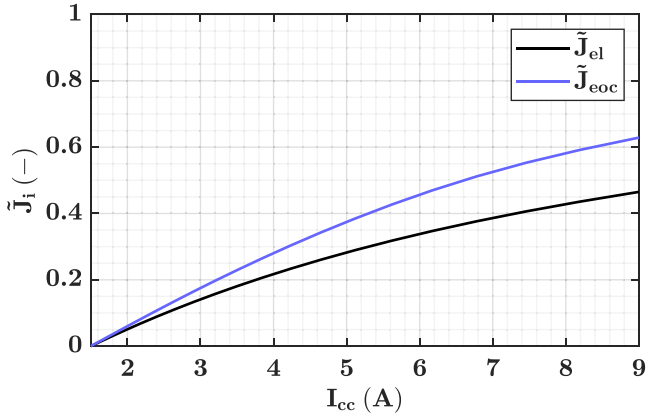

Fig. 5. Evolution of individual normalized cost functions $\tilde{J}_{el}$ and $\tilde{J}_{eoc}$ as a function of CC current I_{cc} of CC–CV charge protocol.

$$\min_{\vec{x}=[I_1,I_2,\ldots,I_3]} \quad f(\vec{x}) \tag{12a}$$

subject to:

$$t_f \leq t_{max}, \tag{12b}$$

$$SOC_f \geq SOC_{min}, \tag{12c}$$

$$T_c(t) \leq T_{max} \qquad \forall t \in [t_0; t_f], \tag{12d}$$

$$\Delta T_c(t) \leq \Delta T_{max} \qquad \forall t \in [t_0; t_f], \tag{12e}$$

$$I_{lb} \leq I_i \leq I_{ub} \qquad \forall i \in [\![1; n]\!], \tag{12f}$$

$$I_m > I_{m+1} > \cdots > I_n \quad \text{with } m \in [\![1; n]\!]. \tag{12g}$$

Differently from previous references in the literature, charge duration is here taken solely as a constraint. Eq. (12b) means that a maximal charging time t_{max} is set, which leads to higher currents and counterbalances the objective function f. This constraint should be chosen between the two bounds of Fig. 4a (29 min and 124 min) for an achievable target in charging time.

The second constraint in Eq. (12c) is on a minimal SOC at end-of-charge SOC_{min}. This constraint compensates the charging time constraint and ensures that a minimum of capacity or energy is charged.

The third and fourth constraints are thermal constraints. Eq. (12d) sets a maximal cell temperature T_{max} to not exceed. Eq. (12e) sets a maximal heating ΔT_{max}, to also limit self-heating at colder temperatures.

The fifth constraint sets bounds on current value in Eq. (12f). A lower bound I_{lb} helps to avoid very low currents that prolongs charging time. An upper bound I_{ub} allows to avoid excessive currents.

Finally, a sixth constraint is used in Eq. (12g) on the regularity of current decrease in the successive steps of the MSCC protocol. The step m where the regularity constraint starts to take effect can be chosen. For example, setting $m = 1$ forces a regular decline from a first step to obtain a current profile similar as [21]. Otherwise, it is possible to set $m > 1$ to let the liberty for an inferior current at beginning-of-charge to obtain a current profile similar to [16].

2.3.3. Optimization algorithm

The optimization is based on the cell model described in 2.2 by linking the Simulink model to the Matlab environment. The optimization algorithm used is the `fmincon` function with the interior points method. The gradients of the objective function and non-linear constraints (Eq. (12b), (12c), (12d) and (12e)) are computed numerically with the central finite differentiation method and are fed to `fmincon` at each iteration. From a given initial value of MSCC currents $\vec{x}_0$, the optimization algorithm thus runs charge simulations to obtain information on objective function, constraints and their gradients, and then decides a new iterates until stopping criteria are met and an optimal solution $\vec{x}_*$ is found.

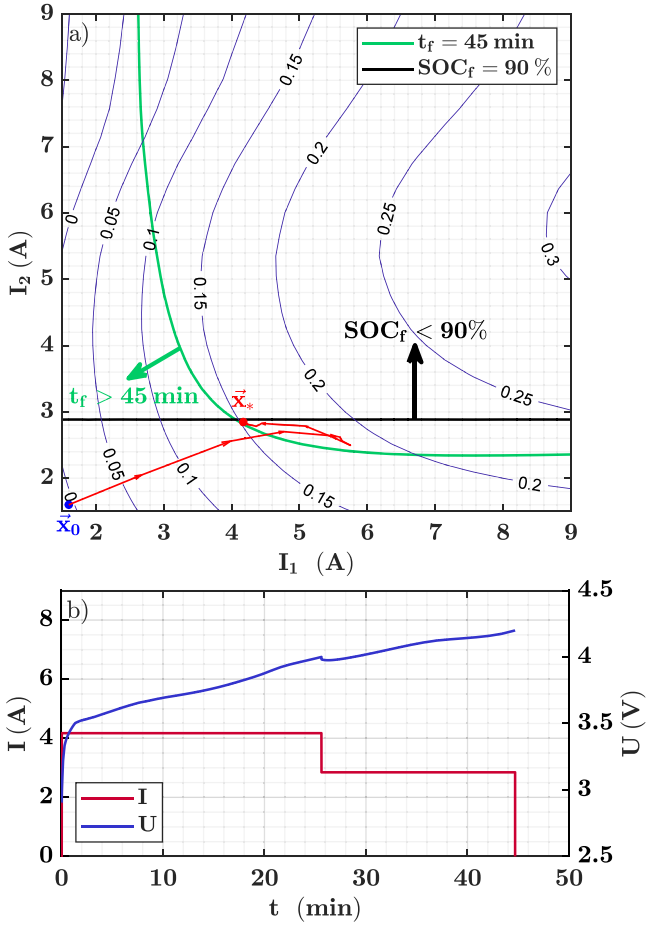

Fig. 6. Example of numerical results for MSCC protocol with 2 steps ($n = 2$, $U_1 = 4.0$ V, $U_2 = 4.2$ V, $\vec{\omega} = [0.8, 0.2]$, $T_{ext} = 25$ °C): (a) contours of the objective function f, constraints on charge duration t_f, and final state-of-charge SOC_f and iterations from initial vector $\vec{x}_0$ to optimal solution $\vec{x}_*$, (b) current and voltage profiles of optimal protocol.

2.4. Example of numerical results

To better understand the operation of the optimization algorithm according to the set of Eq. (12), a case study is proposed with a MSCC protocol of two stages. The two-dimensional case gives an intuition about the influence of constraints on the solution. Two constraints are considered here, one on the charge duration $t_f \leq 45$ min, and the other on the final state-of-charge $SOC_f \geq 90$ %.

Fig. 6a draws the contours of the objective function f and the position of the two constraints. The objective function tends to decrease when both currents I_1 and I_2 decrease. The constraint on the final state-of-charge SOC_f only depends on the current of the last stage I_2. All values of I_2 that are above this constraint do not respect the condition $SOC_f \geq 90$ %. On the other hand, the constraint on the charge duration t_f depends on the value of the current in all stages. All combinations of I_1 and I_2 that are located left and below this constraint do not respect the condition $t_f \leq 45$ min. The feasible solutions are thus combinations of I_1 and I_2 that are located between the two constraints lines in the low-right corner. As f decreases with lower values of I_1 and I_2, the optimal solution to problem 12 is located at the intersection of the two constraints.

Fig. 6 also depicts the iterations of the optimization algorithm from an initial guess $\vec{x}_0$ to the found solution $\vec{x}_*$. It can be seen that the algorithm first seeks to respects all constraints and then seeks to minimize f inside the feasible domain. The final iterate $\vec{x}_*$ is indeed

Table 1
Specifications of the cell investigated in aging tests.

Reference	LG INR18650HG2
Positive material	$LiNi_{0.8}Mn_{0.1}Co_{0.1}O_2$ (NMC)
Negative material	Graphite + SiO (G-SiO)
Nominal capacity	3000 mAh
Energy density	240 Wh kg^{-1}
Voltage range $[U_{min}, U_{max}]$	2.5 to 4.2 V
Charge temperature range	0 to 50 °C
Standard charge current	1.5 A (C/2)
Fast charge current I_{fc}	4 A (1.33C)

found at the intersection of the two constraints. Fig. 6b finally reports the simulated current and voltage profiles of the corresponding optimal protocol.

The same principle holds for a higher number of stages in the MSCC protocol. In the following, this method is exploited to define several fast charging MSCC protocols with 5 or 10 stages as case studies to experimentally investigate the impact of protocols defined by this method on aging.

3. Experimental aging tests

This section describes the experimental tests conducted to verify the impact of optimized MSCC fast charging protocols on battery lifetime. They are compared with fast charging CC–CV protocols, considered as baseline conditions.

3.1. Studied cell

The cell reference INR18650HG2 from LG is selected to conduct aging experiments. Table 1 details its specifications. It is a 3 Ah cell in the 18 650 cylindrical format, with a nickel-rich $LiNi_{0.8}Mn_{0.1}Co_{0.1}O_2$ (NMC) positive electrode and a blended graphite-silicon oxide (G-SiO) negative electrode. Its materials and high energy density make it suited to battery electric vehicles with high driving autonomy.

The manufacturer recommends both a standard charge current and a fast-charge current of respectively 1.5 A (C/2) and 4 A (1.33C). Hence, we expect 4 A to be representative of fast charging for this cell.

3.2. Optimized MSCC and reference CC-CV charging protocols

Five fast charging MSCC protocols are defined by using the numerical optimization problem presented in Section 2 and compared to four reference CC–CV protocols under similar operating conditions.

3.2.1. Common parameters for optimized MSCC protocols

For the definition of optimized MSCC protocols, several parameters are kept constant between all conditions: the voltage thresholds and several constraints.

The number of stages is set to $n = 10$ for cases of complete charge. This number of stages allows sufficient tuning of the current on different SOC ranges while not significantly increasing the convergence time of the optimization algorithm for too small current variations between stages. With the number of stages set to ten, several options can be considered for setting voltage thresholds values U_i such as increments of voltage, or increments of SOC or energy and corresponding changes in the cell OCV. The issue with using, for example, fixed voltage increments between stages is that the first stages are completed very rapidly due to high overvoltages and represent a small portion of the charged capacity, while last stages either significantly extend the charging duration or cut the charge short. Thus, more discretization is needed for the high voltage range. Ultimately, we opted for progressively decreasing voltage increments between each stage which resulted in the voltage thresholds detailed by Table 2. They allow for a high amount of capacity to be charged in the first stages and for adaptation of the current in the last stages in the high voltage range. Moreover, as the cell upper voltage limit U_{max} is progressively reached, no prolonged charging happens at U_{max} such as in a CC–CV protocol. Thus, these thresholds can help to limit aging due to high overvoltages towards end-of-charge. All in all, this choice helps to better balance the three main objectives of low charging time, high capacity charged, and low degradation. The voltage thresholds in Table 2 are related to the specific OCV features of the studied NMC/G-SiO cell, which is relatively linear in its 10%–100% SOC range [43], and should be adapted depending on the electrodes' materials.

Table 2
Voltage thresholds of stages of optimized MSCC protocols.

U_{stage}	Voltage (V)
U_1	3.60
U_2	3.90
U_3	4.00
U_4	4.05
U_5	4.10
U_6	4.12
U_7	4.14
U_8	4.16
U_9	4.18
U_{10}	4.20

To limit aging as well, four constraints are set. Thermal constraints of Eqs. (13) and (14) require the cell temperature to be inferior to 50 °C and to not rise more than 15 °C relative to the ambient temperature. The current levels of each stage are bounded between 300 mA (C/10) and 9 A (3C) as set by Eq. (15). Finally, constraint of Eq. (16) forces the current to decrease regularly starting from the second stage, while current I_1 is let free.

$$T_c(t) \leq 50\ °C \quad \forall t \in [0; t]. \tag{13}$$

$$\Delta T_c(t) \leq 15\ °C \quad \forall t \in [0; t]. \tag{14}$$

$$C/10 \leq I_i \leq 3C \quad \forall i \in [\![1; n]\!]. \tag{15}$$

$$I_2 > I_3 > \cdots > I_n. \tag{16}$$

3.2.2. Experimental conditions for reference and optimized charging protocols

Four CC–CV protocols are selected to offer comparison with MSCC optimized protocols. They were previously investigated in one of our aging studies among other protocols [31]. Their experimental conditions, charge durations and final SOCs are given in Table 3. Three parameters are varied: the ambient temperature T_{ext}, the CC stage current I_{cc}, and the CV stage voltage U_{cv}. The chosen temperatures of 5, 25, and 45 °C represent a cold, mild, and hot climate, respectively. Because of reduced internal resistance when ambient temperature increases, the charge duration decreases and the final state-of-charge increases. Most conditions are achieved at the recommended fast charging current of $I_{cc} = 4$ A (1.33C) during CC stage and at the maximum cell voltage of $U_{cv} = 4.2$ V during CV stage, with charging stopped when the current is lower than $I_{cv} = 300$ mA (C/10), in order to represent near complete charge at the selected temperatures. Parameters I_{cc} and U_{cv} are changed for condition 2, to have one partial charge condition at 25 °C.

Five simulation conditions are given to the optimization algorithm to obtain five optimized MSCC protocols. Three key parameters are modified: the ambient temperature T_{ext}, the constraint on charge duration t_f, and the constraint on final state-of-charge SOC_f. These conditions are summarized in Table 4 as well as the t_f and SOC_f of the

Table 3
Experimental conditions for reference CC–CV protocols and experimentally measured charge duration t_f and final state-of-charge SOC_f.

Condition	T_{ext} (° C)	I_{cc} (A)	U_{cv} (V)	t_f (min)	SOC_f (%)
1	25	4 (1.33C)	4.2	61	96.2
2	25	5 (1.66C)	4.1	46	83.3
3	5	4 (1.33C)	4.2	66	91.4
4	45	4 (1.33C)	4.2	53	97.8

Table 4
Experimental conditions for optimized MSCC protocols and experimentally measured charge duration t_f and final state-of-charge SOC_f.

Condition	T_{ext} (° C)	$t_f \leq$ (min)	$SOC_f \geq$ (%)	n (–)	t_f (min)	SOC_f (%)
MSCC A	25	60	98	10	65	96.8
MSCC B	25	50	98	10	52	93.5
MSCC C	25	35	80	5	37	78.4
MSCC D	5	90	95	10	91	90.4
MSCC E	45	45	98	10	44	95.1

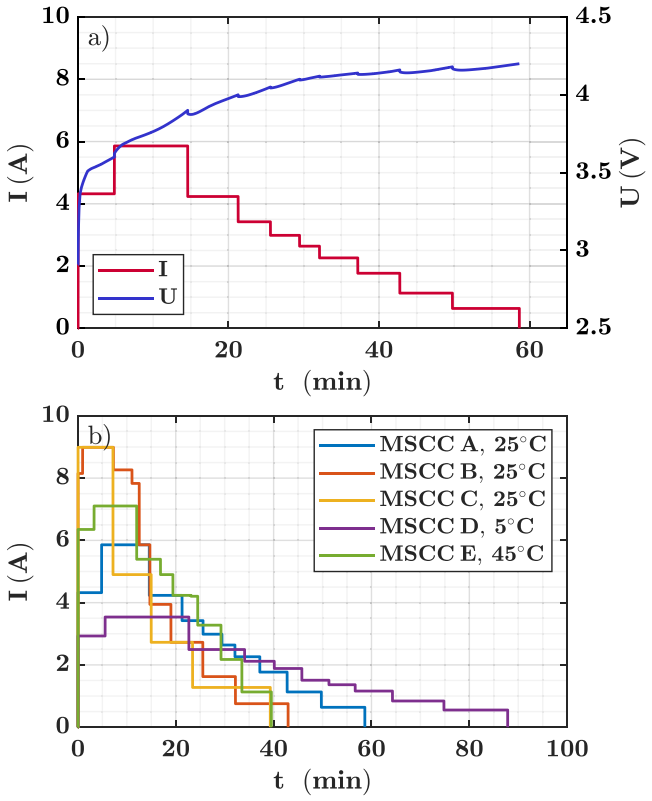

Fig. 7. Optimized MSCC protocols for aging experiments: (a) simulated current and voltage profiles of MSCC A and (b) simulated current profiles of all conditions as a function of charge time.

defined protocols measured in experimental conditions. The simulated current profiles of defined optimized protocols are pictured in Fig. 7b. These conditions are chosen to allow for an objective comparison with fast charging CC–CV protocols (Table 3) in terms of thermal conditions, charge duration and capacity charged, with the objective to either decrease the charge time and/or the degradation compared to CC–CV protocols. Each comparison is explained in the following paragraphs.

3.2.3. Description of the compared charging protocols

Condition CC–CV 1 is considered to investigate the impact of a near complete charge at 25 °C. It is compared to conditions MSCC A and MSCC B, which aim to decrease the degradation in a similar charge duration of around 60 min or to reduce the charge duration to around 50 min, respectively. As an example, simulated current and voltage profiles of MSCC A are shown in Fig. 7a.

Condition CC–CV 2 is considered to treat a case of partial charge at 25 °C. A higher current of $I_{cc} = 5$ A (1.66C) is used in the CC stage and a reduced voltage $U_{cv} = 4.1$ V is used in the CV stage. These parameters lead to a 15 min faster charge than the complete charge at the same ambient temperature but with slightly less capacity charged. It is compared to condition MSCC C, which aims to further decrease the charge duration by 10 min. The number of stages is limited to $n = 5$ in this case, to operate on the same voltage window as its CC–CV reference.

Condition CC–CV 3 is considered to investigate the impact of a near complete charge at a cold temperature of 5 °C. It is compared to condition MSCC D, which aims to decrease the degradation. As previous tests with the CC–CV protocol (charging in 66 min) showed that the cell aged very rapidly [31], the charge duration constraint was relaxed to 90 min.

Condition CC–CV 4 is considered to investigate the impact of a near complete charge at a hot temperature of 45 °C. It is compared to conditions MSCC E, which aims to decrease the charge duration to around 45 min. Thanks to improved kinetics at elevated temperature, this charge duration (while respecting SOC_f constraint) can be reached without touching the upper bound on current, contrarily to condition MSCC B and C at 25 °C (see Fig. 7b).

Five optimized fast charging MSCC protocols are obtained in this manner. Their current profiles are vastly different compared to reference CC–CV protocols (Fig. 7b). Also, several MSCC protocols significantly exceed the maximum current value of 4 A recommended by the cell manufacturer (Table 1). A cycling aging campaign was performed to verify the impact of such protocols on aging.

3.3. Aging tests procedure

Experimental cycle aging tests are performed by repeating a charge-pause–discharge-pause sequence. The charge step is either one of the reference CC–CV protocols (conditions 1, 2, 3, 4) or one of the optimized MSCC protocols (conditions A, B, C, D, E). In total, 9 tests are carried out. Discharges are identical for all tests and are done in a CC protocol with a current of 1.5 A (C/2). Charges and discharges are separated by 15 min pauses to allow the cells to cool down to ambient temperature.

Each test is performed on two different new cells to verify repeatability. All cells were pre-screened. The preliminary inspections showed that cell-to-cell variations in capacity and resistance were low and could be neglected compared to the difference in cycle life caused by different charging protocols. Thus, clear conclusions could be drawn from the comparison of aging caused by optimized MSCC protocols and reference CC–CV protocols.

While considering test equipment, cycling is conducted with Biologic BCS-815 power benches connected electrically to the cells with Biologic BH-1i holders. Cells are placed inside Climats thermal chambers to regulate temperature at the ambient temperature T_{ext}.

3.4. Characterization procedure

Initial, periodic and final characterizations are performed at a temperature of 25 °C. Cycling tests are interrupted around every 10 days for the characterizations. Their goal is to provide a reference measure of capacity and its evolution with aging under comparable conditions. Capacity Q_{dch} is measured during a CC discharge at C/10 until U_{min}, after the cells have been charged by a CC charge at C/10 until U_{max}. The relative capacity based on this measure is used in the following section to assess aging caused by fast charging protocols.

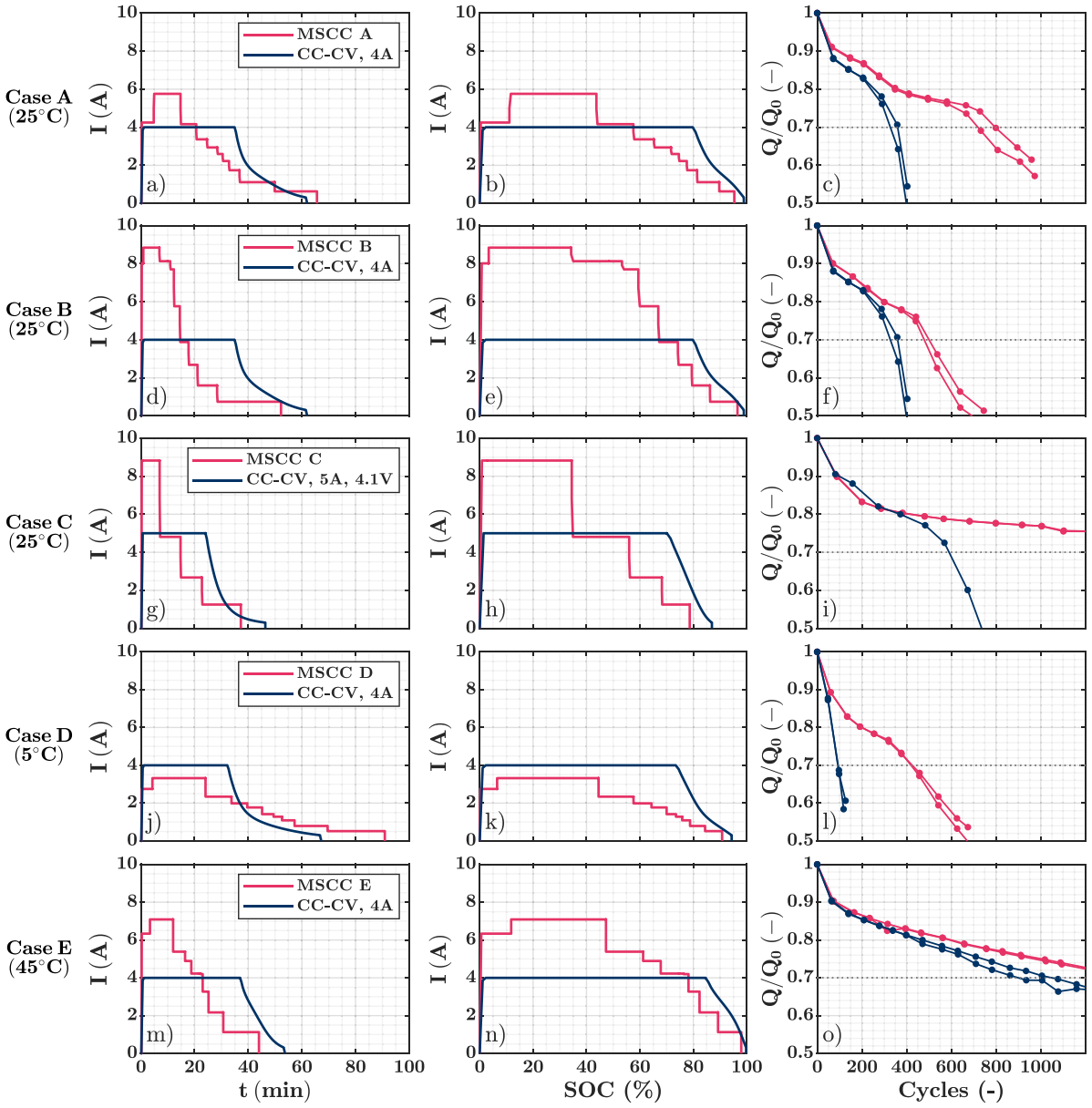

Fig. 8. Comparison of experimental charging and aging results between CC–CV reference protocols and optimized MSCC protocols: (left) charge current as a function of time, (center) charge current as a function of SOC and (right) evolution of relative capacity as a function of cycle number. Each row compares one case of MSCC protocol with a corresponding CC–CV protocol.

4. Experimental aging results and discussions

This section reports the experimental results and further discusses them. Results of optimized MSCC protocols and reference CC–CV protocols are compared on Fig. 8. The two left columns of Fig. 8 compare the charge current profiles, as a function of time and of SOC, for one charge event. The right column reports the evolution of relative capacity as a function of the number of accumulated charge/discharge cycles.

4.1. Case A (25 °C)

The protocol MSCC A is compared with the CC–CV protocol of parameters T_{ext} = 25 °C, I_{cc} = 4 A, U_{cv} = 4.2 V, and I_{cv} = 0.3 A. The current profiles are compared on Fig. 8a and b. Charging time of protocol MSCC A is 65 min, which is 4 min longer than its reference CC–CV protocol. The current of the MSCC protocol becomes inferior to that of CC–CV after a SOC of 58%. This result can be attributed to the cost on end-of-charge overvoltage introduced in 2.3.1.

Evolutions of relative capacity are compared on Fig. 8c. From the beginning of cycling, protocol MSCC A degrades the cell less than the CC–CV protocol, with 3% less capacity loss. The degradation stays inferior to that of CC–CV after that, and the MSCC A protocol even postpones and limits the sharp acceleration of capacity loss caused by CC–CV protocol below a remaining capacity of 80%. This capacity rollover, that can be observed for both protocols, is indicative of lithium plating [44,45]. Thus, although MSCC A protocols did not avoid lithium plating, it allowed to reduce its amount while charging in a similar duration. This result can be attributed to the significant reduction of MSCC current after 58% of SOC. Considering an end-of-life criterion of 70% remaining capacity (30% capacity loss), cells cycled under CC–CV protocol reached end-of-life after around 330 cycles and those cycling with MSCC A between 700 and 800 cycles.

4.2. Case B (25 °C)

The protocol MSCC B is compared to the same CC–CV protocol and their current profiles are compared on Fig. 8d and e. Charge duration of protocol MSCC B is of 52 min, inferior by 9 min to that of its reference CC–CV protocol. To achieve this low charging time, the current values of MSCC A are more than two times superior to that of CC–CV (superior to 8 A) during a significant part of the charge, which corresponds to 53% of the capacity. The current also becomes inferior to that of the CC–CV protocol after 74% of SOC, thus 16% later than MSCC A.

Evolutions of relative capacity are compared on Fig. 8f. When compared with MSCC A (Fig. 8c), it can be seen that the lower charge duration of MSCC B negatively impacts the cycle life. Nevertheless, it can also be observed that the significantly lower charging time and higher currents for 74% of charged capacity did not increase the degradation when compared to the reference CC–CV protocol. After a relatively similar capacity loss at beginning of cycling, the MSCC B gradually degrades less than the CC–CV reference. Cells cycled under MSCC B protocol reached end-of-life after around 450 cycles.

4.3. Case C (25 °C)

The protocol MSCC C is compared to the CC–CV protocol of parameters T_{ext} = 25 °C, I_{cc} = 5 A, U_{cv} = 4.1 V and I_{cv} = 0.3 A. The charge is stopped at a partial SOC for the two protocols. Their current profiles are compared on Fig. 8g and h. The charging time of MSCC C protocol is only 37 min, 9 min lower to that of the CC–CV reference. Current of MSCC C becomes inferior to that of CC–CV after 56 % SOC. The final SOC of protocol MSCC C is lower by 5% compared to that of the CC–CV reference, which can be quite significant considering the impact of depth-of-cycling on aging [46].

Evolutions of relative capacity are compared on Fig. 8i. The degradation caused by the two protocols is similar at the beginning of cycling. At 80% remaining capacity and below, however, the degradation caused by MSCC C considerably slows while that caused by the CC–CV reference sharply increase. This result can potentially be explained by the lower final SOC of MSCC protocol, which cause the cell to charge less on SOC interval where aging mechanisms such as lithium plating can occur. Cells cycled under the CC–CV protocol reached end-of-life after around 600 cycles, whereas cells cycled under MSCC C protocol only lost 25% of their capacity after 1200 cycles.

4.4. Case D (5 °C)

For cases at low temperature, the protocol MSCC D is compared to the CC–CV protocol of parameters T_{ext} = 5 °C, I_{cc} = 4 A, U_{cv} = 4.2 V, and I_{cv} = 0.3 A. Their current profiles are compared on Fig. 8j and k. The charge duration of MSCC D is 91 min, which is 25 min slower than its CC–CV reference. Therefore, the current of MSCC D is always inferior to the CC–CV protocol in the SOC domain.

Evolutions of relative capacity are compared on Fig. 8l. The CC–CV protocols caused massive degradation to the cells, characterized by a sharp drop of capacity. This shows that the studied cell is highly impacted by fast charging at low temperatures. The MSCC D protocol reduced aging significantly. The first part of degradation, characterized by a decrease of the speed of capacity loss, can be observed, similar to results at higher temperatures. Then, at around 75% remaining capacity, the capacity loss accelerates strongly again. All in all, the end-of-life is reached after around 100 cycles for the CC–CV reference and after around 400 cycles for the MSCC D protocol. Thus, an adapted charge duration and lower current rates allowed to significantly improve the cells lifetime.

4.5. Case E (45 °C)

For cases at high temperature, the protocol MSCC E is compared to the CC–CV protocol of parameters T_{ext} = 45 °C, I_{cc} = 4 A, U_{cv} = 4.2 V, and I_{cv} = 0.3 A. Their current profiles are compared on Fig. 8m and n. The MSCC E protocol completes the charge in 44 min, which is 9 min lower compared to the CC–CV reference. The current of MSCC E protocol becomes inferior to that of the CC–CV protocol after a SOC of 78%.

Evolutions of relative capacity are compared on Fig. 8o. The two charge protocols induce a similar degradation, albeit slightly lower for MSCC E. The degradation is rather low and no acceleration of capacity fade can be observed for both conditions. Cells cycled with the CC–CV reference reached end-of-life between 900 and 1000 cycles, while cells cycled with MSCC E lost around 28% of their capacity after 1200 cycles. Both results show that the studied cell is less impacted by fast charging at elevated temperature. Moreover, results of cycling with MSCC E show that it is possible to charge at significantly higher current rates than with CC–CV for a significant portion of the charge without an increase in the degradation.

4.6. Discussions

The experimental results call for discussions on two different topics: the proposed method to optimized fast charging, specifically, and the impact of fast charging on aging, generally.

4.6.1. Proposed method to define fast charging protocols

The main objective of this study was to present new experimental evidence on the possibility to define fast charging protocols, that do not increase aging, with numerical optimization methods. To that end, we used a coupled electro-thermal cell model and proposed an optimization problem with several improvements, to then launch an experimental aging study with optimized fast charging protocols and CC–CV protocols of comparable charge durations and capacities as references.

Results of our experimental study demonstrated that the optimized protocols allowed to reduce charge duration and/or degradation. These results were obtained by employing a frequently used electro-thermal model framework, at the cell level, and without employing an aging model. Instead, aging was taken into account in an implicit manner with simple principles. Firstly, a MSCC protocol is used with a sufficient number of steps to adapt the current during charge and also with increasing voltage thresholds to progressively reach the upper cell voltage. Secondly, a penalty is imposed on high overvoltages when charging on the last graphite phase transition. Thirdly, several reasonable and compatible constraints are set on charge duration, final SOC, temperature, current bounds, and on decreasing currents. This way of proceeding allows to quickly define fast charging protocols for many operating conditions and at a low experimental cost.

The obtained aging results are encouraging for the method. For example, using protocol MSCC A instead of the CC–CV reference protocol more than doubled the cell lifespan (Fig. 8a). They could further be improved by enhancing the cell model or the optimization problem. Possible enhancements include the addition of an aging model, the optimization of voltage thresholds or the adaptation of the fast charging protocols parameters to significant change in the cell SOH.

4.6.2. Impact of fast charging on cell aging

Aging has to be carefully considered to enable fast charging because high currents are known to accelerate several aging mechanisms. Although the optimized protocols of our experimental study were successful in reducing the degradation compared to the CC–CV references, several of these protocols still caused a rather rapid aging, leading to end-of-life in a few hundreds of cycles. This is coherent to the findings of Sieg et al. on another high energy cell [20]. Even when

seeking to charge while avoiding a prominent degradation mechanism such as lithium plating, they found that high currents still caused an important degradation. Therefore, there is a reasonable compromise to be made between low charge duration and high durability. For example, Spingler et al. obtained a drastic improvement in cycle life with an optimized protocol compared to a CC–CV protocol of similar charging time, by allowing for a slightly longer charge time or 75 min [21].

While a trade-off has to be made, our experimental findings nevertheless show that there exist opportunities for higher currents without necessarily reducing cycle life, at least for the high energy NMC/G cell investigated here. One opportunity is to use high currents at low SOC, such as demonstrated by case MSCC B. Indeed, currents more than two times of the recommended maximum current can be used for a significant portion of the charge while still lowering degradation compared to the CC–CV reference (Fig. 8e and f). Another opportunity is to use high currents until a partial state-of-charge or lower end-of-charge voltage, such as shown by case MSCC C (Fig. 8h and i), and results of Mussa et al. [47]. Finally, there is another opportunity for fast charging at elevated temperature such as demonstrated by case MSCC E (Fig. 8n and o). These opportunities are further corroborated with the results or Yang et al. [48], that showed a very high cycle life for a high energy cell by performing a partial fast-charge at elevated temperature and the discharge at a lower temperature.

Therefore, the results suggest the possibility to significantly reduce charging time while still maintaining a good durability by using these strategies.

5. Conclusions

This article proposed a method to define the parameters of battery fast charging protocols by numerical optimization and investigated their impact on durability.

A multi-stage of constant current protocol was chosen because of its straightforward framework and its possibility to adapt the current on different state-of-charge ranges. An electro-thermal model at the cell level was set up to accurately represent the cell dynamics during fast-charge at different temperatures. Based on this model, a constrained optimization problem was formulated. Differently from the literature, this problem considers aging in an implicit manner, in the different costs and constraints. The costs penalized high currents both when the electrical resistance is high, such as at low state-of-charge or low temperature, and when completing the last graphite transition to the fully lithiated stage, at elevated states-of-charge. Then, charging time was considered as a constraint that effectively requires high enough currents to reach the target. The charging time target was further balanced by constraints on charged capacity, temperature, current bounds, and on the decreasing of current during charge with the aim of managing degradation.

The proposed optimization method was then used for an experimental aging study, performed on a high energy lithium-ion cell with a $LiNi_{0.8}Mn_{0.1}Co_{0.1}O_2$ positive electrode and a graphite-silicon oxide negative electrode. Five case studies of optimized multi-stage of constant current protocols were defined by modifying three parameters: the ambient temperature, the charge time constraint, and the charged capacity constraint. These protocols were compared to fast charging constant current–constant voltage protocols as references. The results showed that optimized protocols can either improve the cell cycle life in a similar charging time, sometimes by more than two-fold, or decrease the charge time without increasing the degradation. It was also observed that there exist opportunities for significantly higher currents at low state-of-charge, with a partial charge, and at elevated temperature.

These results suggest that the proposed optimization method can be used to define fast charging protocols with a lower impact on cycle life. Moreover, charge time can be further reduced while maintaining a good cycle life by using the discussed strategies.

Glossary

SEI	Solid electrolyte interphase
SOC	State-of-charge
SOH	State-of-health
CC–CV	Constant current–constant voltage
MSCC	Multi-stage of constant-current
CC	Constant-current
CV	Constant-voltage
NMC	Lithium nickel manganese cobalt oxide
G	Graphite
SiO	Silicon oxide

CRediT authorship contribution statement

Romain Mathieu: Conceptualization, Methodology, Software, Formal analysis, Investigation, Writing - original draft, Writing - review & editing, Visualization. **Olivier Briat:** Conceptualization, Methodology, Resources, Writing - review & editing, Supervision, Project administration, Funding acquisition. **Philippe Gyan:** Conceptualization, Methodology, Resources, Writing - review & editing, Supervision, Project administration, Funding acquisition. **Jean-Michel Vinassa:** Conceptualization, Methodology, Resources, Writing - review & editing, Supervision, Project administration, Funding acquisition.

Declaration of competing interest

The authors declare that they have no known competing financial interests or personal relationships that could have appeared to influence the work reported in this paper.

Acknowledgments

This work received funding from the French National Association for Technological Research (ANRT) under grant CIFRE N° 2016/1200. The funding source had no involvement in any aspect of the study or report.

Appendix A. Supplementary data

Supplementary material related to this article can be found online at https://doi.org/10.1016/j.est.2021.102756.

References

[1] Till Bunsen, P. Cazzola, L. D'Amore, M. Gorner, S. Scheffer, R. Schuitmaker, H. Signollet, J. Tattini, J.T.L. Paoli, Global EV Outlook 2019 to Electric Mobility, Tech. rep., International Energy Agency, 2019.

[2] S. Ahmed, I. Bloom, A.N. Jansen, T. Tanim, E.J. Dufek, A. Pesaran, A. Burnham, R.B. Carlson, F. Dias, K. Hardy, M. Keyser, C. Kreuzer, A. Markel, A. Meintz, C. Michelbacher, M. Mohanpurkar, P.A. Nelson, D.C. Robertson, D. Scoffield, M. Shirk, T. Stephens, R. Vijayagopal, J. Zhang, Enabling fast charging – A battery technology gap assessment, J. Power Sources 367 (2017) 250–262, http://dx.doi.org/10.1016/j.jpowsour.2017.06.055.

[3] M. Keyser, A. Pesaran, Q. Li, S. Santhanagopalan, K. Smith, E. Wood, S. Ahmed, I. Bloom, E. Dufek, M. Shirk, A. Meintz, C. Kreuzer, C. Michelbacher, A. Burnham, T. Stephens, J. Francfort, B. Carlson, J. Zhang, R. Vijayagopal, K. Hardy, F. Dias, M. Mohanpurkar, D. Scoffield, A.N. Jansen, T. Tanim, A. Markel, Enabling fast charging – Battery thermal considerations, J. Power Sources 367 (2017) 228–236, http://dx.doi.org/10.1016/j.jpowsour.2017.07.009.

[4] M. Abdel-Monem, K. Trad, N. Omar, OmarHegazy, B. Mantels, G. Mulder, P.V.-d. Bossche, Joeri Van Mierlo, Lithium-ion batteries: Evalution study of different charging methodologies based on aging process, Appl. Energy 152. http://dx.doi.org/10.1016/j.apenergy.2015.02.064.

[5] P. Keil, A. Jossen, Charging protocols for lithium-ion batteries and their impact on cycle life-an experimental study with different 18650 high-power cells, J. Energy Storage 6 (2016) 125–141, http://dx.doi.org/10.1016/j.est.2016.02.005.

[6] S.S. Zhang, The effect of the charging protocol on the cycle life of a li-ion battery, J. Power Sources 161 (June) (2006) 1385–1391, http://dx.doi.org/10.1016/j.jpowsour.2006.06.040.

[7] N. Omar, M.A. Monem, Y. Firouz, J. Salminen, J. Smekens, O. Hegazy, H. Gaulous, G. Mulder, P. Van den Bossche, T. Coosemans, J. Van Mierlo, Lithium iron phosphate based battery - Assessment of the aging parameters and development of cycle life model, Appl. Energy 113 (2014) 1575–1585, http://dx.doi.org/10.1016/j.apenergy.2013.09.003.

[8] T. Waldmann, B.I. Hogg, M. Wohlfahrt-Mehrens, Li plating as unwanted side reaction in commercial Li-ion cells – A review, J. Power Sources 384 (February) (2018) 107–124, http://dx.doi.org/10.1016/j.jpowsour.2018.02.063.

[9] S.J. An, J. Li, C. Daniel, D. Mohanty, S. Nagpure, D.L. Wood, The state of understanding of the lithium-ion-battery graphite solid electrolyte interphase (SEI) and its relationship to formation cycling, Carbon 105 (2016) 52–76, http://dx.doi.org/10.1016/j.carbon.2016.04.008.

[10] I. Laresgoiti, S. Käbitz, M. Ecker, D.U. Sauer, Modeling mechanical degradation in lithium ion batteries during cycling : Solid electrolyte interphase fracture, J. Power Sources 300 (2015) 112–122, http://dx.doi.org/10.1016/j.jpowsour.2015.09.033.

[11] S. Zhang, Chemomechanical modeling of lithiation-induced failure in high-volume-change electrode materials for lithium ion batteries, npj Comput. Mater. 3 (1) (2017) 1–11, http://dx.doi.org/10.1038/s41524-017-0009-z.

[12] X. Fleury, M.H. Noh, S. Geniès, P.X. Thivel, C. Lefrou, Y. Bultel, Fast-charging of lithium iron phosphate battery with ohmic-drop compensation method: Ageing study, J. Energy Storage 16 (2018) 21–36, http://dx.doi.org/10.1016/j.est.2017.12.015.

[13] M. Abdel-Monem, K. Trad, N. Omar, O. Hegazy, P. Van den Bossche, J. Van Mierlo, Influence analysis of static and dynamic fast-charging current profiles on ageing performance of commercial lithium-ion batteries, Energy 120 (2017) (2017) 179–191, http://dx.doi.org/10.1016/j.energy.2016.12.110.

[14] C. Zhang, J. Jiang, Y. Gao, W. Zhang, Q. Liu, X. Hu, Charging optimization in lithium-ion batteries based on temperature rise and charge time, Appl. Energy 194 (2017) 569–577, http://dx.doi.org/10.1016/j.apenergy.2016.10.059.

[15] S. Schindler, M. Bauer, H. Cheetamun, M.A. Danzer, Fast charging of lithium-ion cells: Identification of aging-minimal current profiles using a design of experiment approach and a mechanistic degradation analysis, J. Energy Storage 19 (March) (2018) 364–378, http://dx.doi.org/10.1016/j.est.2018.08.002.

[16] Z. Guo, B. Yann, X. Qiu, L. Gao, C. Zhang, Optimal charging method for lithium ion batteries using a universal voltage protocol accommodating aging, J. Power Sources 274 (2015) 957–964, http://dx.doi.org/10.1016/j.jpowsour.2014.10.185.

[17] H.E. Perez, X. Hu, S. Dey, S.J. Moura, Optimal charging of Li-ion batteries with coupled electro-thermal-aging dynamics, IEEE Trans. Veh. Technol. 66 (9) (2017) 7761–7770, http://dx.doi.org/10.1109/TVT.2017.2676044.

[18] T. Waldmann, M. Kasper, M. Wohlfahrt-Mehrens, Optimization of charging strategy by prevention of lithium deposition on anodes in high-energy lithium-ion batteries - electrochemical experiments, Electrochim. Acta 178 (2015) 525–532, http://dx.doi.org/10.1016/j.electacta.2015.08.056.

[19] T. Amietszajew, E. McTurk, J. Fleming, R. Bhagat, Understanding the limits of rapid charging using instrumented commercial 18650 high-energy Li-ion cells, Electrochim. Acta 263 (2018) 346–352, http://dx.doi.org/10.1016/j.electacta.2018.01.076.

[20] J. Sieg, J. Bandlow, T. Mitsch, D. Dragicevic, T. Materna, B. Spier, H. Witzenhausen, M. Ecker, D.U. Sauer, Fast charging of an electric vehicle lithium-ion battery at the limit of the lithium deposition process, J. Power Sources 427 (2019) 260–270, http://dx.doi.org/10.1016/j.jpowsour.2019.226846.

[21] F.B. Spingler, W. Wittmann, J. Sturm, B. Rieger, A. Jossen, Optimum fast charging of lithium-ion pouch cells based on local volume expansion criteria, J. Power Sources 393 (February) (2018) 152–160, http://dx.doi.org/10.1016/j.jpowsour.2018.04.095.

[22] U.R. Koleti, C. Zhang, R. Malik, T.Q. Dinh, J. Marco, The development of optimal charging strategies for lithium-ion batteries to prevent the onset of lithium plating at low ambient temperatures, J. Energy Storage 24 (June). http://dx.doi.org/10.1016/j.est.2019.100798.

[23] Y.H. Liu, C.H. Hsieh, Y.F. Luo, Search for an optimal five-step charging pattern for li-ion batteries using consecutive orthogonal arrays, IEEE Trans. Energy Convers. 26 (2) (2011) 654–661, http://dx.doi.org/10.1109/TEC.2010.2103077.

[24] T.T. Vo, X. Chen, W. Shen, A. Kapoor, New charging strategy for lithium-ion batteries based on the integration of Taguchi method and state of charge estimation, J. Power Sources 273 (2015) 413–422, http://dx.doi.org/10.1016/j.jpowsour.2014.09.108.

[25] A. Abdollahi, X. Han, N. Raghunathan, B. Pattipati, B. Balasingam, K. Pattipati, Y. Bar-Shalom, B. Card, Optimal charging for general equivalent electrical battery model, and battery life management, J. Energy Storage 9 (2017) 47–58, http://dx.doi.org/10.1016/j.est.2016.11.002.

[26] K. Liu, K. Li, Z. Yang, C. Zhang, J. Deng, Battery optimal charging strategy based on a coupled thermoelectric model, Electrochem. Acta 225 (2017) 330–344, http://dx.doi.org/10.1109/CEC.2016.7748334.

[27] R. Suresh, R. Rengaswamy, Modeling and control of battery systems. Part II: A model predictive controller for optimal charging, Comput. Chem. Eng. 119 (2018) 326–335, http://dx.doi.org/10.1016/j.compchemeng.2018.08.017.

[28] X. Lin, X. Hao, Z. Liu, W. Jia, Health conscious fast charging of Li-ion batteries via a single particle model with aging mechanisms, J. Power Sources 400 (May) (2018) 305–316, http://dx.doi.org/10.1016/j.jpowsour.2018.08.030.

[29] M.R. Palacín, Understanding ageing in Li-ion batteries: A chemical issue, Chem. Soc. Rev. 47 (13) (2018) 4924–4933, http://dx.doi.org/10.1039/c7cs00889a.

[30] X.G. Yang, C.Y. Wang, Understanding the trilemma of fast charging, energy density and cycle life of lithium-ion batteries, J. Power Sources 402 (September) (2018) 489–498, http://dx.doi.org/10.1016/j.jpowsour.2018.09.069.

[31] R. Mathieu, O. Briat, P. Gyan, J.-M. Vinassa, Comparison of the impact of fast charging on the cycle life of three lithium-ion cells under several parameters of charge protocol and temperatures, Appl. Energy 283 http://dx.doi.org/10.1016/j.apenergy.2020.116344.

[32] R. Mathieu, O. Briat, P. Gyan, J.-M. Vinassa, Electro-thermal behavior of four fast charging protocols for a lithium-ion cell at different temperatures, in: Proceedings: IECON 2018-44th Annual Conference of the IEEE Industrial Electronics Society, IEEE, 2018, http://dx.doi.org/10.1109/IECON.2018.8591603.

[33] X. Lin, H.E. Perez, S. Mohan, J.B. Siegel, A.G. Stefanopoulou, Y. Ding, M.P. Castanier, A lumped-parameter electro-thermal model for cylindrical batteries, J. Power Sources 257 (2014) 1–11, http://dx.doi.org/10.1016/j.jpowsour.2014.01.097.

[34] N. Damay, C. Forgez, M.-p. Bichat, G. Friedrich, Thermal modeling of large prismatic LiFePO 4 / graphite battery. Coupled thermal and heat generation models for characterization and simulation, J. Power Sources 283 (2015) 37–45, http://dx.doi.org/10.1016/j.jpowsour.2015.02.091.

[35] Y.C. Zhang, O. Briat, L. Boulon, J.Y. Deletage, C. Martin, F. Coccetti, J.M. Vinassa, Non-isothermal Ragone plots of Li-ion cells from datasheet and galvanostatic discharge tests, Appl. Energy 247 (2019) 703–715, http://dx.doi.org/10.1016/j.apenergy.2019.04.027.

[36] A. Farmann, D.U. Sauer, Comparative study of reduced order equivalent circuit models for on-board state-of-available-power prediction of lithium-ion batteries in electric vehicles, Appl. Energy 225 (April) (2018) 1102–1122, http://dx.doi.org/10.1016/j.apenergy.2018.05.066.

[37] C.R. Birkl, E. McTurk, M.R. Roberts, P.G. Bruce, D.A. Howey, A parametric open circuit voltage model for lithium ion batteries, J. Electrochem. Soc. 162 (12) (2015) A2271–A2280, http://dx.doi.org/10.1149/2.0331512jes.

[38] C. Forgez, D. Vinh Do, G. Friedrich, M. Morcrette, C. Delacourt, Thermal modeling of a cylindrical LiFePO4/graphite lithium-ion battery, J. Power Sources 195 (9) (2010) 2961–2968, http://dx.doi.org/10.1016/j.jpowsour.2009.10.105.

[39] K.E. Thomas, J. Newman, Heats of mixing and of entropy in porous insertion electrodes, J. Power Sources 119–121 (2003) 844–849, http://dx.doi.org/10.1016/S0378-7753(03)00283-0.

[40] J. Nocedal, S.J. Wright, Numerical Optimization, Springer, New York, 2006, http://dx.doi.org/10.1007/978-0-387-40065-5.

[41] M. Dubarry, C. Truchot, B.Y. Liaw, Synthesize battery degradation modes via a diagnostic and prognostic model, J. Power Sources 219 (2012) 204–216, http://dx.doi.org/10.1016/j.jpowsour.2012.07.016.

[42] M. Heß, Kinetics and Stage Transitions of Graphite for Lithium-Ion Batteries (Ph.D. thesis), Swiss Federal Institute of Technology of Zurich, 2013, http://dx.doi.org/10.3929/ethz-a-010000442.

[43] T.T.D. Nguyen, S. Abada, A. Lecocq, J. Bernard, M. Petit, G. Marlair, S. Grugeon, S. Laruelle, Understanding the thermal runaway of ni-rich lithium-ion batteries, World Electr. Veh. J. 10 (4). http://dx.doi.org/10.3390/wevj10040079.

[44] S.F. Schuster, T. Bach, E. Fleder, J. Müller, M. Brand, G. Sextl, A. Jossen, Nonlinear aging characteristics of lithium-ion cells under different operational conditions, J. Energy Storage 1 (1) (2015) 44–53, http://dx.doi.org/10.1016/j.est.2015.05.003.

[45] M. Dubarry, G. Baure, D. Anseán, Perspective on state-of-health determination in lithium-ion batteries, J. Electrochem. Energy Convers. Storage 17 (4). http://dx.doi.org/10.1115/1.4045008.

[46] J. Wang, J. Purewal, J. Graetz, S. Soukiazian, H. Tataria, M.W. Verbrugge, Degradation of lithium ion batteries employing graphite negatives and nickel-cobalt-manganese oxide + spinel manganese oxide positives: Part 2, chemical–mechanical degradation model, J. Power Sources 272 (2014) 1154–1161, http://dx.doi.org/10.1016/j.jpowsour.2014.07.028.

[47] A.S. Mussa, M. Klett, M. Behm, G. Lindbergh, R.W. Lindström, Fast-charging to a partial state of charge in lithium-ion batteries: A comparative ageing study, J. Energy Storage 13 (2017) 325–333, http://dx.doi.org/10.1016/j.est.2017.07.004.

[48] X.-g. Yang, T. Liu, S. Ge, Y. Leng, D. Wang, X.-g. Yang, T. Liu, Y. Gao, S. Ge, Y. Leng, D. Wang, Asymmetric temperature modulation for extreme fast charging of lithium-ion batteries asymmetric temperature modulation for extreme fast charging of lithium-ion batteries, Joule 3 (2019) 1–18, http://dx.doi.org/10.1016/j.joule.2019.09.021.